

A laser induced cavitation pump

G R Wang^{1,3}, J G Santiago¹, M G Mungal¹, B Young²
and S Papademetriou²

¹ Mechanical Engineering Department, Stanford University, Stanford, CA 94305-3032, USA

² Selva Medical Inc., Belmont, CA 94002, USA

E-mail: gw@cfdr.com

Received 21 December 2003

Published 4 June 2004

Online at stacks.iop.org/JMM/14/1037

doi:10.1088/0960-1317/14/7/026

Abstract

We demonstrate and discuss a liquid pumping effect based on the interaction between periodically generated cavitation microbubbles and a millimeter diameter tube. The bubbles are generated by the heat of laser adsorption at the tip of an optical fiber immersed in liquid. When the bubbles are generated well away from the tube, a steady streaming flow with a relatively large and energetic ring vortex is observed. Coaxial placement of the fiber within the tube, with the fiber tip near one end of the tube, results in relatively weak pumping of liquid. In contrast, placement of the fiber outside the tube with a similar fiber tip position results in a synergetic and strong pumping effect. This paper presents quantitative measures of pumping performance as a function of relevant parameters including the axial fiber tip position, fiber orientation and laser duty cycle.

1. Introduction

The availability of miniaturized, robust liquid pumping devices should enable the development of a variety of biochemical analyses, electronics cooling systems and other microfluidic devices. The performance demands of biochemical analysis systems are especially challenging in that pumping strategies may need to cope with non-Newtonian liquids and multiphase flow, while dealing with the challenges posed by biofouling. One illustrative example of biomedical instruments which use miniaturized pumping schemes includes the commercially available ISTAT system which analyzes the chemistry of whole blood samples and uses a simple plunger/membrane strategy to achieve pumping of both the calibrant liquids and the sample [1]. For biomedical applications, Endovasix Inc. has recently developed a new micro-biomedical device to break and remove blood clots located in the brain of stroke victims; stroke being the third main cause of death in the United States. In their device, vapor bubbles are produced by heating blood through the absorption of pulsed laser light [2, 3] and micropumping is achieved using a miniature tube device. Pumping with large flow rates is important for the removal of the clots, since the duration of the process is a critical aspect of the clinical application.

Cooling of microelectronics poses a challenge in that the pump should have a fast temporal response and would benefit from use of liquids with a wide variety of thermophysical properties such as heat of vaporization, freezing point and boiling point. An example effort in this area is a series of electroosmotic (EO) pumps currently under development for high heat rate electronics cooling applications [4]. One recently described pump can generate maximum flow rates and pressure capacities of 33 ml min⁻¹ and 1.3 atm, respectively, at 100 V applied potentials [5, 6].

A variety of miniaturized pump strategies have been developed to address the need for robust, miniaturized pumping devices [7]. A wide variety of actuation schemes have been employed including piezoelectric membranes [8], electrostatic membranes [9], thermopneumatic actuators [10], electromagnetic actuators [11, 12] and ultrasonic flexural plate waves [13]. Field-driven flow pumps with no solid moving parts include electrohydrodynamic [14], magnetohydrodynamic [15] and the EO pumps described earlier.

Two types of miniature pumps effecting fluid pumping are related to the present work. The first is based on periodically and asymmetrically produced microbubbles in a microchannel as demonstrated in [16–20]. The original microbubble resulting from heating is used in ink jet printer mechanisms [21, 22]. The second pump uses a piezoelectric plate to

³ Present address: CFD Research Corporation, 215 Wynn Drive, Huntsville, AL 35805, USA

generate an acoustic streaming flow [23–25]. However, the latter designs result in pressure heads of less than, e.g. 15 mm H₂O [24], and promising applications have not yet been identified [26]. To our knowledge, no combination of the bubble pumping and steady streaming has been investigated.

In this paper, we experimentally study the pumping performance of laser-induced cavitation bubbles with no moving (solid) parts. The pumping effect is based on a synergistic interaction between steady streaming resulting from laser-induced cavitation bubbles and the dynamics of periodic expanding/collapsing bubbles near a small tube end. The corresponding pumping effect provides flow rates in excess of 0.9 ml min⁻¹ and maximum pressure heads of about 76 mm H₂O. This study also provides experimental validation data for modeling efforts.

2. Experimental setup

Figure 1(a) shows the experimental setup used for the flow experiments. The experiment was conducted in a plexiglass rectangular reservoir of size 60 × 40 × 20 mm³, filled with a blood analog working fluid, which is a mixture of Red Dye #2, water, glycerin and Xanthum gum. This mixture simulates the optical and viscoelastic property of blood [27] and has relatively high absorption coefficient for the laser wavelength of 532 nm used here. This mixture was used because the experiment presented here is part of a larger study of the dynamics of a laser-induced cavitation device, which is used to break and remove blood clots in the brain. Proper operation of the clot treatment device requires significant pumping of blood and other liquids.

The current study used the mixture of the viscoelastic liquid contained within the reservoir, a small glass tube and an optical fiber. A 50 μm diameter optical fiber coupled to the laser was inserted into the reservoir through its sidewall and the connection was sealed with a hemostasis valve from Qosina Corp. Inside the reservoir, the fiber was placed coaxially to a 12 mm long glass tube with a 1 mm inner diameter. The relative position between the tube end and fiber tip in this setup can be adjusted by a three-dimensional micropositioning stage from Newport Corp. The coordinate system of the tube/fiber is shown in figure 1(b).

A Nd:YAG laser with a wavelength of 532 nm designed and built by Endovasix Inc. was used to deliver light pulses through the fiber at a frequency of 5 kHz. The duration of each laser pulse was about 30 ns. In the operation of this device, laser light is absorbed and converted into heat, which results in the periodic formation of vapor bubbles near the tip of the fiber. The laser duty cycle is controllable as discussed below.

4 μm diameter fluorescent particles with peak absorption and emission wavelengths of 660 and 680 nm (Molecular Probes Inc.), respectively, were used as a flow seed for visualization. Excitation of the fluorescent beads was accomplished using a He–Ne laser of 30 mW with a wavelength of 632 nm. At the outlet of the laser, a 25.4 mm focal length cylindrical lens was used to obtain a thin light sheet in the reservoir. A circular lens with long focal length behind a cylindrical lens was used to focus the light sheet to a 100 μm thickness. Optical filters with a collection band in the 675–685 nm range were used to filter away the noise of

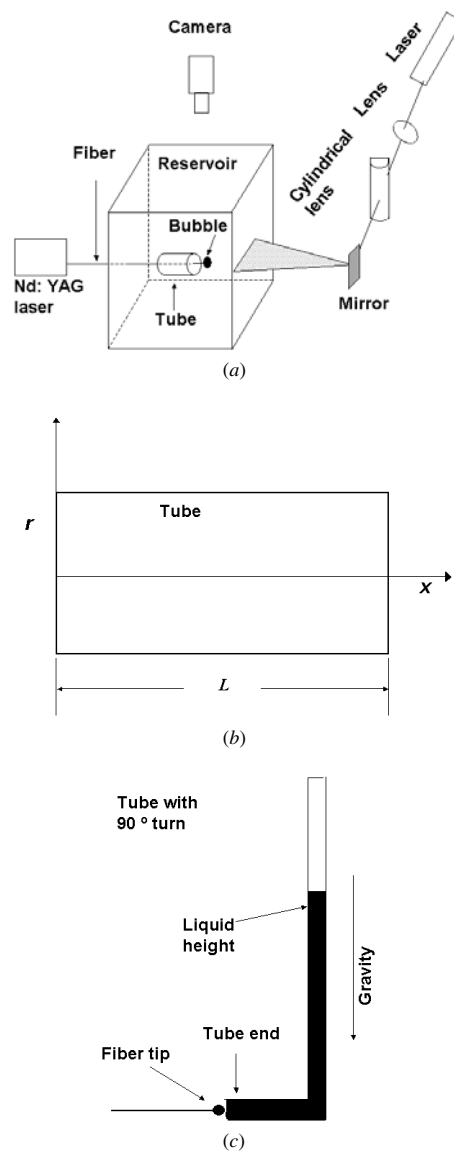


Figure 1. Experimental setup: (a) schematic of test section and optical diagnostic system. (b) Coordinate system of the fiber and tube assembly. (c) Manometer tube arrangement used for the measurement of pressure and flow rate.

the laser light from both the Nd:YAG laser and He–Ne laser. Despite this filtering, however, the emission light due to the pulsed laser in the region of highest absorption (near the fiber tip) was captured by the imaging system. To further improve the quality of the image, a small piece of black paper was placed on the filter to block laser-flare and prevent blooming in the CCD array.

In addition to fluorescent particle pathline visualizations, images of elastic and inelastic light scattering were used to characterize bubble dynamics and were captured using diffuse illumination. A xenon flash lamp (Perkin Elmer, model FX-1163) was used for this purpose, triggered by a timing box (model DG 535, Stanford Research Systems Inc.), and synchronized with the Nd:YAG laser. The flash duration was 0.9 μs. Since the lifetime of bubble from the beginning of expansion to the end of collapse was of the order of 70 μs, and the camera sampling rate only 3.7 frames s⁻¹, we obtained

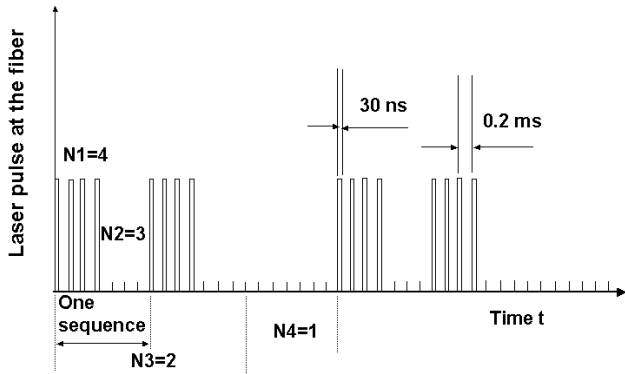


Figure 2. Duty cycle parameter used for laser firings. Duty cycle specification is of the form $DCP(N1, N2, N3, N4)$. Example cycle of $DCP(4, 3, 2, 1)$ is shown. $N1$ represents the number of active pulses to the fiber; $N2$ is the number of inactive pulse cycles. $N3$ represents the number of complete active sequences; $N4$ denotes the number of complete inactive sequences.

only one image per bubble cycle in these images. However, the bubble dynamics are highly repeatable and periodic. Thus, using timing delays on the flash lamp, we explored the bubbles at equal phase (to verify periodicity) and at different phases to record the evolution dynamics of the bubble growth and collapse.

A MicroMax 1300YHS-DIF CCD camera from Princeton Instruments with maximum continuous sampling rate of $3.7 \text{ frames s}^{-1}$ was used to image the flow field. Exposure times varying from 40 to 1000 ms were used. The camera was mounted on an upright microscope (Eclipse 400 Nikon Inc.) with objectives of $1\times$, $2\times$ and $10\times$ magnification.

Figure 1(c) shows the device used to quantify the pressure head and flow rate generated by the laser-induced cavitation bubble pump. A glass tube with an inner diameter of 1 mm and a 90° turn on one end was placed so that the end open to the liquid reservoir is coaxial to the fiber. The relative position between the tube end and fiber tip was adjusted using the three-dimensional translation stage. The rise of the free surface of the liquid in the vertical portion of this pump tube was used to estimate pump pressure capacity. The rate of change of this height was used as a measure of the pump flow rate. Note that the velocity of the water in the manometer tube was low enough such that the hydrostatic pressure of the water column was at all times approximately equal to the pressure load on the pump. That is, for the flow rates of interest, the pressure drop due to viscous losses in the tube was negligible.

The laser duty cycle parameters (DCP) can be described in terms of four numbers: $DCP(N1, N2, N3, N4)$, as illustrated in figure 2. The parameters $N1, N2, N3$ and $N4$ take the values of 4, 3, 2 and 1 respectively as an example for illustration in figure 2. $N1$ and $N2$ are respectively the number of repeated active laser pulses (termed ‘ON’ states of the fiber) and the number of repeated inactive laser pulses (termed ‘OFF’ states of the fiber). The periods $N1$ and $N2$ define the basic sequence of the pulse train pattern. $N3$ and $N4$ respectively denote the number of the sequences activated (i.e., an ‘ON’ sequence) and deactivated (i.e., an ‘OFF’ sequence resulting in no heating) respectively. Thus, the higher the $N1$, the more the input power to the fluid, and the higher $N2$ and $N4$, the less the input power to the fluid. The power input into the fluid is dependent on $N1$,

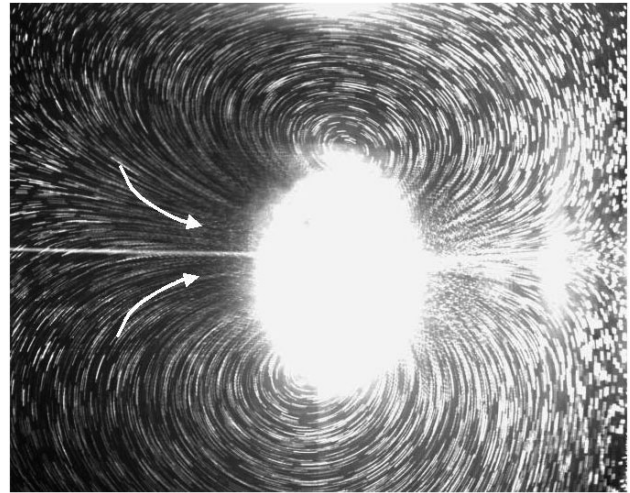


Figure 3. Steady streaming of a ring vortex produced by the periodic expansion and collapse of bubbles with a duty cycle of $DCP(100, 250, 1, 0)$ and pulse energy of $E = 300 \mu\text{J}$. The height of this imaged region is 8 mm. The arrows show the streaming direction. The bright area in the middle is noise from laser beam. The straight bright line entering from the left side of the image is the fiber. Camera exposure time is 1 s.

$N2, N3$ and $N4$, and the energy of each pulse, E . In this paper, $N3$ and $N4$ are always constant at 1 and 0, respectively.

In all experiments, we did not detect mechanical damage due to cavitation to the tube’s inner surface. (Note that the majority of our experiments were conducted with the fiber placed coaxially within the tube so that, in most cases, the bubble collapsed toward the fiber tip and not toward the tube.) Close inspection of the optical fiber tip did show that cavitation cycles do have a measurable effect on the fiber tip surface. Fibers used in experiments had a surface that was dull in appearance compared to a newly-cleaved fiber which has specular facets. However, note that, after this initial ‘breaking in’ period, the optical fiber operation was very robust, repeatable for as many as 2 h of operation (approximately 2 million pulses). Also, fibers used in experiments had undetectable changes in length during the course of the experiment.

3. Experimental results

3.1. Visualization results

We will consider first the case of laser firing of the fiber in the absence of the tube. The bubble dynamics for this case has been described by Molho *et al* [28]. There is a periodic movement of the liquid near the bubble surface that is in a direction of the radial expansion and collapse. However, the average velocity field of the liquid within a few diameters of a bubble generated at a fiber optic tip is not radial or reciprocal in nature. This is shown by the particle pathline visualization shown in figure 3. The figure shows an induced steady streaming consisting of a relatively large ring vortex. The pulse duty cycle in this experiment was $DCP(100, 200, 1, 0)$ with each pulse having an energy of $300 \mu\text{J}$. The arrows drawn over the image show the direction of steady streaming as determined by un-aliased movies of the particle motion

in a region a few diameters from the fiber tip. The camera exposure time was 1 s. The bright straight line entering the image from the left of the approximate center of the image is the fiber and the field of view of this visualization is $11 \times 8 \text{ mm}^2$. The bright area in the middle of the image is light emission (and perhaps a minor amount of elastic scatter) of both particles and background bulk liquid, which is excited by the YAG laser beam as it exits the fiber. This emission was strong enough to corrupt the image despite the color filters. The fluid near the fiber tip was observed in real-time to move away from the fiber face.

Although the laser fired periodically, the resulting fluid motion throughout the observable field was steady. This strongly suggests that acoustic streaming [29] results from the periodic disturbance, caused by the bubbles near the fiber. This implies that periodic laser firing at a free fiber tip (i.e. no influence of the presence of an external wall, tube, etc) can produce a pumping effect. The velocity magnitudes of the streaming and the size and shape of the ring vortex should depend on the duty cycle DCP, energy of each laser pulse E , pulse width, laser wavelength and working fluid. Presumably, the pumping action should be more pronounced with increasing NI and E , and less pronounced with increasing $N2$.

Next, let us consider the influence of the tube on the velocity field near the fiber tip ($x/L = 1$). In figure 4, the fiber is placed coaxially within an unbent, straight tube with the fiber tip centered with the tube and at the exit plane of the tube. The other end of the tube (not shown in the image) is also submerged within and open to the liquid in the reservoir. The horizontal tube and fiber enter the image from the left. A vertical stripe just visible from the tube end and extending to the bottom of the image is a shadow caused by illumination light scatter from the end of the tube. The DCP was (10, 250, 1, 0) and E was $300 \mu\text{J}$. The field of view is $6 \times 8 \text{ mm}^2$ and the camera exposure time is 1 s. The direction of steady streaming is denoted by the arrow drawn over the image. At this fiber tip/tube orientation, there is again a steady streaming of the flow and a ring vortex surrounds the region of the fiber tip, as with the free fiber experiment. However, in this case the streaming direction is opposite to that of a free fiber (e.g., compare figures 3 and 4). Given that figure 3 represents the case of a fiber protruding well beyond a tube end ($x/L \gg 1$) and figure 4 represents the fiber located at the tube end ($x/L = 1$), and these have opposite rotational motion, there should be a critical value of x/L where the steady streaming changes its direction [30]. This is in fact the case and indicates that the presence of the tube, as in the case of figure 4, can cause a flow that is opposite to and stronger than the acoustic streaming generated with the free fiber tip. The flow field near the tube tip can also produce a pumping pressure head within the tube as we shall see in the discussions below. This result agrees qualitatively with the model of Yuan and Prosperetti [17] which predicts that if a bubble is produced at a single location inside a microtube (and near one end), there is a pumping effect and the flow moves to the other side of the tube end.

More interesting, however, is the case when the fiber was placed near the left end of the tube, i.e. at $x/L = 0$, as shown in figure 5. The figure shows pathline visualization of steady streaming for this case. As in the case of the configuration

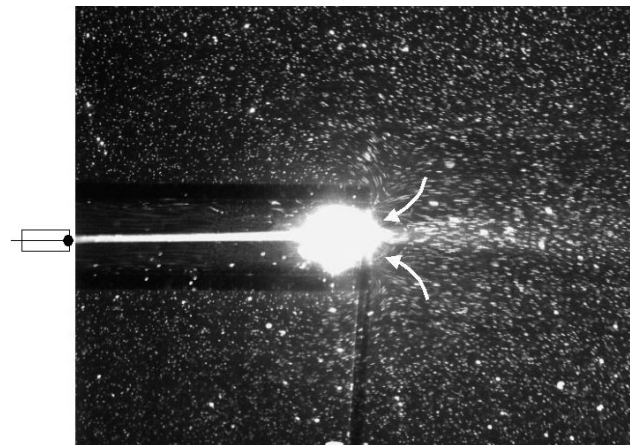


Figure 4. Relatively weak pumping action when the fiber tip is placed within and near the right end of the tube. The height of this imaged region is 5 mm. The arrows indicate streaming direction. The bright line on the left side is the fiber within the tube. The line from the tube end to the bottom of the picture is a shadow (the region is illuminated from the top). The camera exposure time is 1 s.

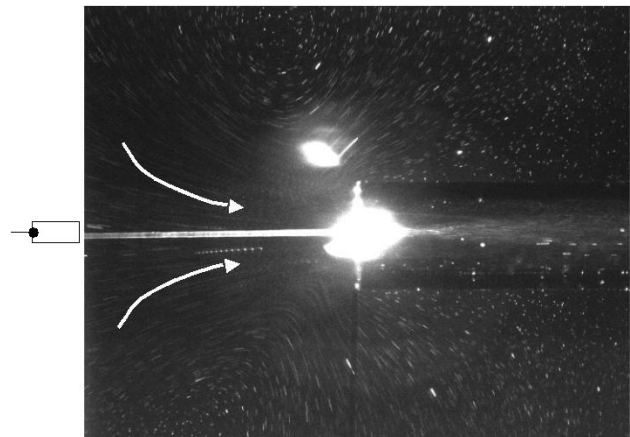


Figure 5. Relatively strong synergistic pumping effect when the fiber tip is placed near the left end of the tube. The height of this imaged region is 5 mm. The arrows indicate the streaming direction. The bright line on the left side is the fiber and the dark areas on the right side are the tube walls. The line from the tube end to the bottom of the picture is a shadow, and the bright area above the tube end is light scatter. The camera exposure time is 1 s.

shown in figure 4, water again pumps into the tube end. The main difference between this case and that of figure 4, however, is the degree to which the flow is pumped. The observed velocities (and flow rates within the tube) were much higher for this case. Note that the particle pathline streaks are obtained using the same exposure time of 1 s so that streak length is proportional to local velocity. Note that the pumping direction into the tube is, for the last configuration, consistent with the liquid pumping near a free fiber tip (which is away from the tip), so that the effects of the fiber tip and the tube seem to be complementary only in this configuration.

In the following section, we quantify the pumping characteristics for the configuration shown in figure 5. We measure the induced pressure head as a function of the fiber tip position, E , NI and $N2$.

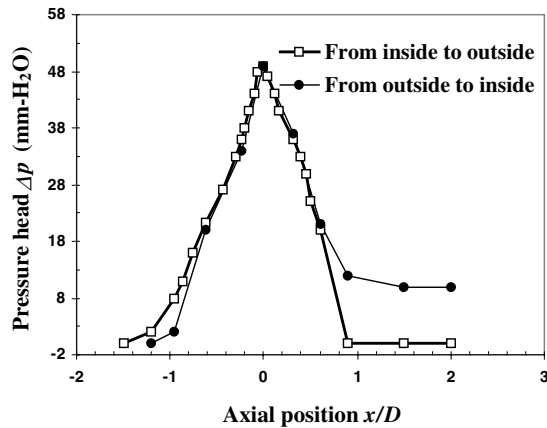


Figure 6. Relation between pressure head and axial position near the left tube end with fiber along the tube axis. E was $300 \mu\text{J}$ and DCP was (250, 200, 1, 0). The symbol \square denotes measurements obtained for a fiber moving from the inside to the outside of the tube. The symbol \bullet represents measurements obtained for a fiber moving from the outside to inside of the tube.

3.2. Pressure head results

All measurements in figures 6–11 for pressure head were repeatable. In all cases, the curves presented are averages of 3–5 realizations. Since the liquid is a complex blood analog and its density is about 1050 kg m^{-3} , units of $\text{mm H}_2\text{O}$ are used here to approximately express the pressure head. The pressure head induced by the tube was measured for various positions of the fiber tip. Near the left end of the tube ($x/D = 0$) the induced pressure head Δp was very sensitive to the axial position of the tip within a range of $|x| < 2D$, where D is the tube inner diameter. This is shown in figure 6, where the fiber was placed along the tube axis with $E = 300 \mu\text{J}$ and DCP(250, 200, 1, 0). The negative x -coordinate in figure 6 corresponds to positions where the fiber tip was placed outside the left end of the tube (see figure 1(b)). Initially the fiber tip was placed inside the tube at $x/D = 5$ with no measurable pressure rise. The pressure rise was zero until x/D decreased to a value of $x/D = 0.6$, where further translation of the fiber tip resulted in pressure heads of $10 \text{ mm H}_2\text{O}$ and larger. Further translation of the fiber tip resulted in a sharp increase in Δp to a maximum value of $50 \text{ mm H}_2\text{O}$ at $x/D = 0$. We should also note that at this location the acoustic nature of the sound clearly changed (unfortunately no acoustic measurements have been made to date). As the fiber tip was further moved away from the left end of the tube to negative values of x/D , Δp rapidly decreased again until $x/D = -1.5$ where Δp was nearly zero. With further movement of the fiber to left, the measured pressure head remained zero.

The measured pressure head was repeatable as a function of fiber tip location but was also a function of the history of the tip position. This is shown as a second experimental curve in figure 6 for the case where the fiber tip was moved from $x/D = -1.5$ toward higher values of x/D . For this direction of translation, when x/D was larger than unity, Δp was approximately $10 \text{ mm H}_2\text{O}$ (compared to the zero values measured before). This behavior indicates that there was a hysteresis flow phenomenon associated with fiber tip translation. Irrespective of this hysteresis, figure 6 shows that

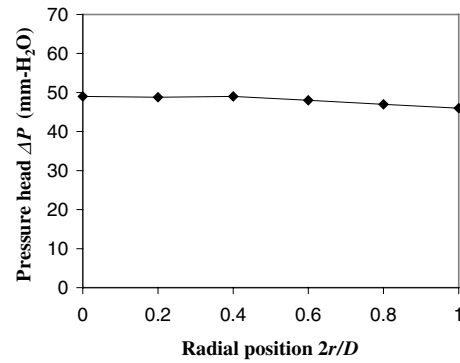


Figure 7. Relation between pressure head and radial position at $x/D = 0$. $E = 300 \mu\text{J}$ and the duty cycle was DCP = (250, 200, 1, 0). Radial position has negligible effect on generated pressure.

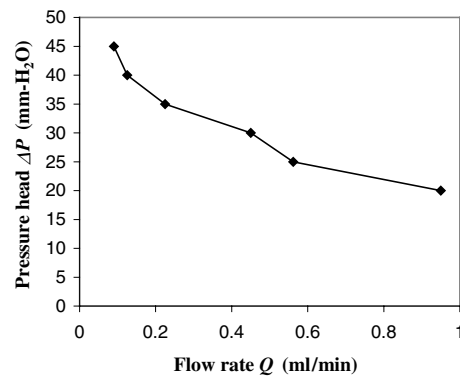


Figure 8. Relationship between pressure head Δp and flow rate Q at $x/D = 0$ and $2r/D = 0$. For this case, $E = 300 \mu\text{J}$ and the duty cycle was DCP(250, 200, 1, 0). Pressure is roughly inversely proportional to flow rate.

Δp is much higher at the tube end than inside the tube, and the pressure head produced is a strong function of x/D . Each of the measured pressure measurements in this figure reflects steady state pressure values achieved by the pump at each fiber position. Also, a similar result was achieved when the order in which the measurements were taken was reversed.

Compared to the influence of axial position on Δp , radial position is not as important a parameter. This is shown in figure 7 where the fiber tip is placed at $x/D = 0$ and values of $E = 300 \mu\text{J}$ and DCP(250, 200, 1, 0) were used. In this figure, r denotes the radial position of the fiber tip within the tube. At the $2r/D = 0$ radial position, $\Delta p = 49 \text{ mm H}_2\text{O}$. At the wall ($2r/D = 1$), $\Delta p = 46 \text{ mm H}_2\text{O}$, which is only a 6% variation. In the next sections, we present only measurements of Δp at $x/D = 0$ and $2r/D = 0$.

Figure 8 shows the relation between Δp and flow rate Q at $x/D = 0$ and $2r/D = 0$, for $E = 300 \mu\text{J}$ and DCP(250, 200, 1, 0). The measurements show that Δp decreases with increasing Q , as is typical of fluid pumps, although an ideal linear dependence of Q on Δp was not observed. For Δp of $20 \text{ mm H}_2\text{O}$, Q is 0.95 ml min^{-1} . This value is impressive given the compact geometry of the device. Presumably, the flow rate can be increased using designs with multiple tubes in parallel.

The relationship between Δp and laser pulse energy E for a given DCP is shown in figure 9, for DCP(100, 80, 1, 0)

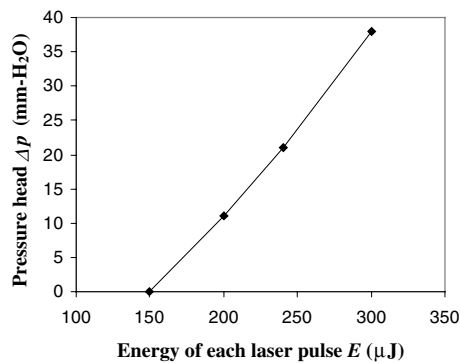


Figure 9. Relation between pressure head Δp and energy of each laser pulse E at $x/D = 0$ and $2r/D = 0$. Duty cycle was DCP(100, 80, 1, 0). Pressure head is highly sensitive to laser pulse energy.

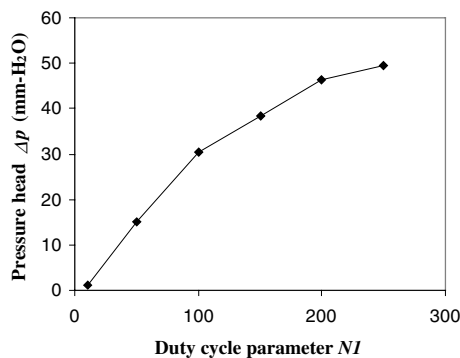


Figure 10. Relation between Δp and duty cycle parameter NI for $E = 300 \mu\text{J}$ and a fixed $N2$ value of 200 at $x/D = 0$ and $2r/D = 0$.

and a fiber location of $x/D = 0$ and $2r/D = 0$. The results show that for the power range used in this experiment, Δp increases linearly with E . At $E = 150 \mu\text{J}$, Δp is nearly zero, while $E = 300 \mu\text{J}$ produces a pressure head of $\Delta p = 38 \text{ mm H}_2\text{O}$. No apparent saturation for Δp is observed here as E is increased, implying that further increases in E may result in higher pressure head.

The zero pressure point in figure 9 suggests a minimum required pulse energy of approximately $150 \mu\text{J}$. We believe this may be the minimum energy required to form a bubble in this fiber/tube system. For example, if we assume constant values for heat capacity and heat of vaporization of 4.2 J gK^{-1} and 2300 J g^{-1} , respectively, a $150 \mu\text{J}$ vaporization energy corresponds to roughly $1200 \mu\text{m}^3$ volume of liquid. This volume is of the order of the smallest observed bubbles and of the order of the high light scatter region in figure 5.

Figure 10 shows measurements of Δp versus NI for fixed values of $E = 300 \mu\text{J}$ and $N2 = 200$ with a fiber position of $x/D = 0$ and $2r/D = 0$. Since NI denotes the number of laser firings, the higher the NI , the higher the time-averaged power delivered to the liquid. As expected, Δp increases with NI for a given $N2$. Note that Δp increases with increasing NI , but there is a trend toward saturation. We also found that when NI was 10, Δp was about $1 \text{ mm H}_2\text{O}$. Under this condition, NI of 10 corresponds approximately to the minimum value to have a Δp greater than zero.

We found pressure head Δp decreased with $N2$ for given NI and E . Figure 11 shows the relation between Δp and $N2$ for fixed $NI = 250$ and $E = 300 \mu\text{J}$ with a fiber position of

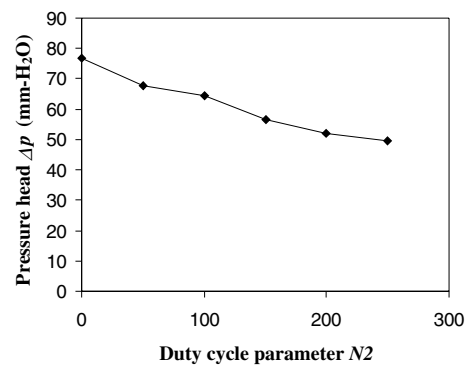


Figure 11. Dependence of pressure head Δp on duty cycle parameter $N2$ for a fixed NI value of 250 and $E = 300 \mu\text{J}$ at $x/D = 0$ and $2r/D = 0$.

$x/D = 0$ and $2r/D = 0$. In figure 11, Δp decreased with the increase in $N2$. Compared with the result in figure 10, however, figure 11 indicates that the sensitivity of Δp to $N2$ is not as high as that of Δp to NI . For instance, in figure 10, with the increase in NI from 0 to 250 for a given $N2 = 200$, Δp increases from 0 to $49 \text{ mm H}_2\text{O}$, an average $\Delta p/NI$ ratio of $0.19 \text{ mm H}_2\text{O}$. In figure 11, with the increase in $N2$ from 0 to 250 for a given NI of 250, Δp decreased from 76 to $49 \text{ mm H}_2\text{O}$. This corresponds to an average $|\Delta p/N2| = 0.1 \text{ mm H}_2\text{O}$. Choice of NI and $N2$ is strongly influenced by any concerns of heating of the fluid (e.g., as in biomedical applications).

Due to the complex physical process between the bubble dynamics and the streaming, Δp also depends on the ratio $NI/N2$ and the absolute value of $|NI - N2|$. For example, figure 12 shows the changes in Δp with $N2$ for three different values of $NI/N2$ (1.25, 1.00 and 0.50) with the fiber at $x/D = 0$ and $2r/D = 0$, and $E = 300 \mu\text{J}$. Note that the power input into the liquid from the laser is fixed when $NI/N2$ is a constant for a given E . Notable in figure 12 is that, even if the ratio $NI/N2$ is constant, Δp increases with increasing $N2$ (or increasing $|NI - N2|$). For example, in the case of $NI/N2 = 1.25$, Δp increases from $28 \text{ mm H}_2\text{O}$ to $50 \text{ mm H}_2\text{O}$, corresponding to an increase in $N2$ from 20 to 200. Even though Δp decreases with an increase in $N2$ as shown in figure 11, Δp increases with $N2$, as shown in figure 12. The reason for this is that each curve corresponds to a fixed value of $NI/N2$, and so NI is not a constant as in the case of figure 11; NI increases with the increase in $N2$, as does the value of $|NI - N2|$. The measurement in figure 12 indicates that Δp depends not only on the input laser power, but also on the value of $N2$ (or $|NI - N2|$) for a given $NI/N2$. This provides more opportunity to manipulate and control Δp . For example, to increase Δp for a given E and power input within the experimental range studied here, NI (and so $N2$) should be increased.

In figure 12, there is a trend of saturation in Δp with increasing $N2$. The saturation is most apparent for small values of $NI/N2$. The highest pressure curve corresponding to $NI/N2 = 1.25$ in figure 12 does not show a strong saturation. However, the lowest curve corresponding to $NI/N2 = 0.5$ exhibits a relatively strong saturation trend. We can therefore conclude that the smaller the value of $NI/N2$, the stronger the saturation.

Another result is shown in figure 13. Here E was 300 and $240 \mu\text{J}$ for the upper and lower pressure curves, respectively.

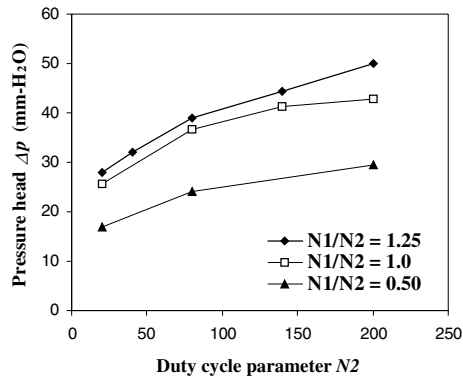


Figure 12. Relation between pressure head Δp and duty cycle parameter N_2 for various values of the ratio N_1/N_2 with $E = 300 \mu\text{J}$, $x/D = 0$ and $2r/D = 0$.

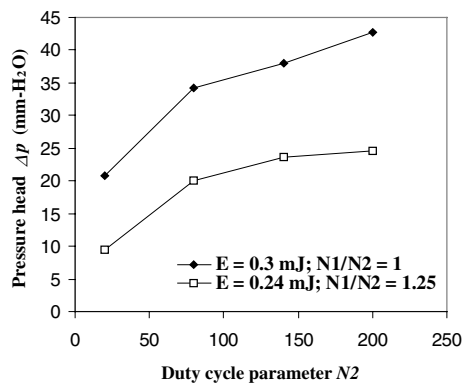


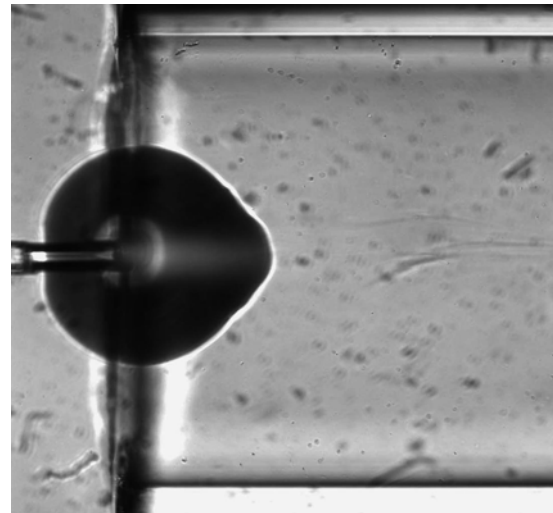
Figure 13. Relation between pressure head Δp and duty cycle parameter N_2 for a constant value of $EN_1/N_2 = 300 \mu\text{J}$ and two values of E at $x/D = 0$ and $2r/D = 0$.

The ratios of N_1/N_2 are not the same for these two cases. The values of N_1/N_2 are 1 and 1.25 for $E = 300 \mu\text{J}$ and $240 \mu\text{J}$, respectively. For a given N_2 , therefore, the value of input power, EN_1/N_2 , is a constant for the two curves. The values of Δp corresponding to $300 \mu\text{J}$ are higher than those corresponding to the $240 \mu\text{J}$ experiment. For instance, at $N_2 = 200$, Δp for $E = 300 \mu\text{J}$ is $42 \text{ mm H}_2\text{O}$, but Δp for $E = 240 \mu\text{J}$ is only $24 \text{ mm H}_2\text{O}$. This indicates that Δp not only depends on the power input EN_1/N_2 , but also depends on E for a given EN_1/N_2 , and that Δp is more sensitive to E than N_1 . In short, figures 10, 11 and 13 all indicate that the most effective parameter that influences Δp is E (and not input power). Note that in figure 13, for each given E , Δp increases with N_2 . This is identical to the result in figure 12.

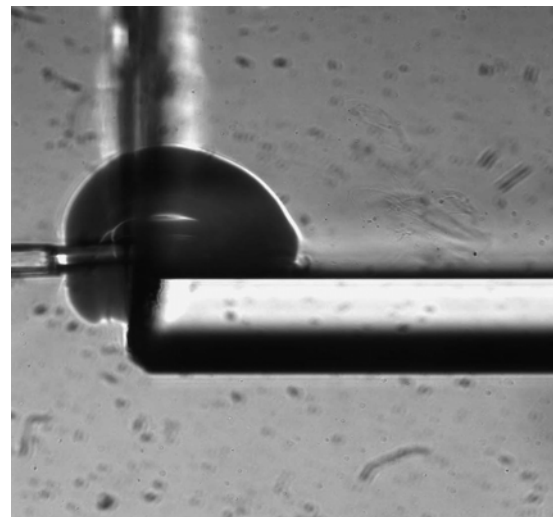
4. Discussion

4.1. Steady streaming

There have been many publications on laser-induced cavitation investigating acoustics, bubble dynamics and cavitation damage in the fields of physics, engineering and tissue cutting for biomedical applications [31, 32]. In these studies, a laser beam is focused on liquids contained in vessels without a fiber body to interact with the flow. To our knowledge, there is no report that such laser-induced cavitation flows can also



(a)



(b)

Figure 14. Maximum bubble size and shape for two different radial positions at $x/D = 0$. Fiber enters the tube end from the left. The inner diameter of the tube is 1 mm and the outer diameter of the fiber is $65 \mu\text{m}$ (including cladding and jacket). (a) The fiber tip at $2r/D = 0$. (b) Fiber at the wall of the tube, $2r/D = 1$.

induce steady streaming with a ring vortex similar to acoustic streaming as shown here, although Vogel *et al* [33] produced the bubble near a solid wall. The reason for this may be that either the forcing frequencies used were too low, or previous studies did not contain asymmetries in the axial direction as is the case here due to the presence of fiber face.

4.2. Effect of bubble size on pressure head

Although intuition may suggest that pressure head should increase with bubble size, this trend is not apparent in our data when the bubbles are generated at different positions. Compare, for example, the bubble images shown in figures 14(a) and (b). For the latter, the fiber is positioned at $2r/D = 1$; for the former, the fiber is positioned at $2r/D = 0$. The bubble is the dark quasi-sphere and semisphere area in figures 14(a) and (b) respectively. The bubble geometry

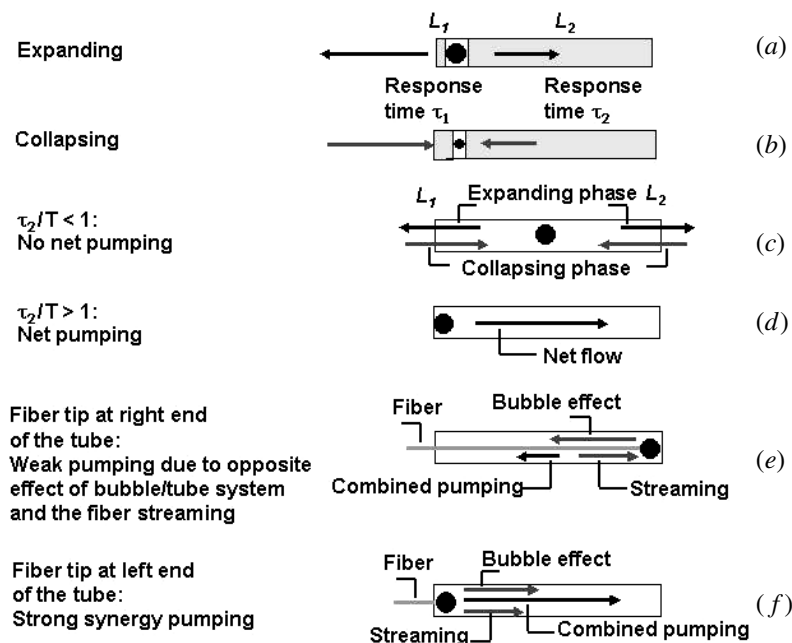


Figure 15. Model of the pumping mechanism (see text for discussion). (a) Expansion phase; (b) collapse phase; (c) no net pumping; (d) net pumping in one direction; (e) weak pumping due to opposing effects of bubble/tube system and fiber and (f) strong synergistic pumping.

is strongly deformed when the fiber is positioned at the wall as shown in figure 14(b) compared to that in figure 14(a). Although the bubbles in these two cases are different, we estimate the bubble volume in figure 14(a) is approximately 1.4 times the bubble volume in figure 14(b). However, the flow associated pressure in figure 14(a) is only 1.06 times that in figure 14(b). For different fiber positions, bubble growth dynamics, local heat transfer and streaming dynamics can be severely changed by the influence of nearby walls and so intuition based on bubble size alone seems to fail.

4.3. Description of pumping dynamics

As mentioned earlier, the experimental results presented here qualitatively support the models of Yuan and Prosperetti [17] and Ory *et al* [18] for a single-bubble case, but only in regions outside the central axial locations of the tube $0.3 < x/L < 0.7$. For example, the experimental setup used for figures 4 and 5 is similar to the situations used in these models for a single bubble in a small tube connecting two reservoirs having the same pressure. In such configurations, liquid is pumped in the direction of the long liquid slug—the tube region opposite to the site of bubbles.

Some differences between the models in [17] and [18], and the present experiment warrant discussion even for bubbles outside the central axial region. For instance, the model in [17] is assumed valid provided the liquid slug length is much larger than tube diameter and all the results presented in that work are in the range of $1 < x/D$ and $x/L < 0.5$. The limitations of this assumption may be apparent as the bubble position approaches the tube end, where their model shows what is probably an artifact divergence in the pumping velocity solutions (see figure 8 in that reference). In the present work, the pumping action we observe is strongest only when the liquid slug is much smaller than the tube diameter, in the

range of $-1 < x/D < 1$ as shown in figure 6. Furthermore, the pressure head achieves its maximum value only when bubbles are produced at the end of the tube, where the left side liquid slug length is zero.

One interesting effect observed in our experiment, not seen in previous models, is a bubble quenching phenomenon that occurs under certain conditions. If the fiber tip is located in the range of $x/L = 0.3–0.7$, pumping occurs immediately after the firing sequences are initiated. However, after about 3 min of pumping, the bubble disappears (or at least was not detected) and pumping flow rate reduces to negligible values. The reason for this quenching effect is not yet clear.

Another apparent difference between our experiments and previous modeling in [17] is the relative size of our bubbles. In the current experiments, the maximum bubble diameter is smaller than the tube inner diameter, so that the bubble is not forced to elongate inside the tube. Also, the presence and orientation of the optical fiber are critical in our experiments. For example, we observe the strongest pumping action when the fiber and tube are oriented such that the steady streaming direction of a fiber without a tube (as in figure 3) complements the pumping caused by the fiber/tube coupling (as in figure 5). In contrast, the work of Yuan and Prosperetti considers only a point source of bubble generation.

The timescales of the current experiment are also clearly much different from the model of Jun and Kim [16], which assumed that evaporation takes place at the hot end of the vapor bubble and condensation takes place at the cold end. They considered a heating pulse width of the order of 1 s. In our experiments, bubbles expand and collapse in a 70–100 μs period and at nearly the same local position.

In this section, we present an illustrative, qualitative description of the effects of the tube/fiber/bubble system. The circles in figure 15 denote bubbles. L_1 and L_2 are the liquid slug length on each side of the bubble. Figures 15(a)–(d)

represent interactions between a bubble and the tube alone, in the absence of a fiber, which we call the simple bubble effect. Figures 15(a) and (b) denote the bubble expansion and collapse phases, respectively. Liquid slugs L_1 and L_2 have respective response times τ_1 and τ_2 in which to change flow direction, while the bubble actuation period is T . If a bubble is produced at $x/L = 0.5$, then $\tau_1/\tau_2 = 1$, and no pumping is produced. For a bubble at the left end of the tube, $\tau_2 \gg \tau_1$. If $\tau_2/T < 1$ (and so $\tau_1/T < 1$) as indicated in figure 15(c), both L_1 and L_2 can respond to flow direction changes during the expansion and collapse phases, no flow rectification is possible and pumping is negligible. This is consistent with the observation that no pumping is observed when NI is sufficiently small as indicated in figure 10. Note that the actual period T for producing bubbles is inversely proportional to $NI/(NI + N2)$.

If $\tau_2/T > 1$, the slug L_2 has insufficient time to respond to the expansion/collapse process. This presumably aids in continuous pumping as illustrated in figure 15(d). Throughout the parameter range we investigated, the larger τ_2/T , the higher the induced pumping velocity and pressure head. This is consistent with the observation that pressure head increases with NI , as shown in figure 10. The pressure head and flow rate produced also depend on the value of L_1/L_2 (and so τ_1/τ_2). The smaller L_1/L_2 (corresponding to a bubble near the left end of the tube), the higher the pumping velocity. The maximum pressure head occurs for a bubble at the end of the tube as shown in figure 6.

If the presence of the fiber is considered, the total pumping effect is determined by the interaction of the fiber steady streaming effect (figure 3) and the simple bubble/tube effects discussed above (figures 15(e) and (f)). When the fiber is oriented such that the fiber steady streaming direction is opposite to the pumping of the simple bubble effect, the net pumping action is reduced as the two effects partially cancel out, as shown in figure 15(e). However, if the fiber steady streaming is in the same velocity direction as the simple bubble effect, a synergy between both flow phenomenon results in strong pumping action as shown in figure 15(f). These weak and strong pumping cases are shown clearly in figures 4 and 5, respectively.

4.4. Improvement

As is the case for several thermal-bubble actuated pumps [7], thermodynamic efficiency of the present pump is low and estimated to be $5 \times 10^{-4}\%$. The thermodynamic efficiency of the pump was defined as the maximum hydraulic power generated by the pump, $[Q\Delta p]_{\max}$, divided by the laser fluence power input into the liquid, P :

$$\eta = [Q\Delta p]_{\max} / P.$$

Here we assume that all the laser fluence is absorbed and converted to heat.

However, its main advantage for designers of microfluidic systems is not in power conversion but in that the pump produces a flow rate large compared to its own volume. The tube/fiber system can pump its own volume every 0.6 s at a 0.95 ml min^{-1} flow rate shown in figure 8. Several other methods can also perhaps be used to produce bubbles other than the laser-induced cavitation used in this study, such as ultrasound and ionic Joule heating, and some of these may

result in increased efficiency. Since the viscosity of the working fluid used here is relatively high (about four times larger than that of water) [27], the flow rate would presumably be improved if a fluid with low viscosity is used. A liquid with low boiling temperature (and/or lower heat of vaporization) could also improve the pump performance. In any such system, the temperature of the working fluid at the position where bubbles are produced should be near the boiling point in order to reduce the energy required to boil liquid. Lastly, flow rate can easily be increased by applying multiple tubes in parallel, and pressure can presumably be increased by pumps arranged in series.

5. Summary and conclusions

There is a steady streaming of liquid flow when vapor bubbles are produced through periodic laser-induced cavitation at the tip of an optical fiber. This effect can be used for pumping liquids using a combined tube/fiber/bubble device. A fiber immersed by itself in a relatively large liquid chamber effects steady streaming such that a ring vortex pumps liquid away from the fiber face. When the fiber is inserted into the left end of a small tube and its tip is placed near the right end, a steady streaming is produced and the flow direction is opposite to the steady streaming case without the tube. Relatively weak pumping is generated inside the tube for this configuration. However, if the fiber tip is positioned near the left tube end, the flow direction is the same as the steady streaming direction in the absence of the tube, and there is a large synergistic pumping effect.

We observed that the pressure head produced is very sensitive to the axial position near the tube end and its maximum value occurs for tip positions near the left end of the tube. At this position, a device created with a $50 \mu\text{m}$ diameter fiber and a 1 mm diameter tube can provide a flow rate of the order of 1 ml min^{-1} . The device can pump its own volume at a rate of 1.2 Hz. This micropumping device may find applications in a variety of microfluidic applications such as electronics cooling or biomedical systems.

Acknowledgments

The authors express their appreciation to Dr Victor Esch from Endovasix Inc. for providing material and equipment for this study and discussion. They also thank machinist Lakhbir Johal in Stanford University for fabrication of the vessel. The first author also thanks his colleague, Dr Josh Molho (now in Caliper Technology) and Dr Shankar Devasenathipathy of Stanford University for very helpful discussion and help during the experiment. Helpful discussions with Professor A Prosperetti from The Johns Hopkins University and Dr M Versluis from the University of Twente are also appreciated. This work was funded by Endovasix Inc, Belmont, CA 94002, USA.

References

- [1] Erickson K A and Wilding P 1993 Evaluation of a novel point-of-care system, the i-STAT portable clinical analyzer *Clin. Chem.* **39** 283–7

- [2] Hebert S J, Levine M A, Sucgang E U, Tran Q Q and Esch V C 2001 Flexible flow apparatus and method for the disruption of occlusions *US Patent Specification* 6,210,400
- [3] Esch V C, Tran Q Q, Anderson R R, Hebert S J, Levine M A and Sucgang E U 2001 Flow apparatus for the disruption of occlusions *US Patent Specification* 6,139,543
- [4] Jiang L N *et al* 2002 Closed-loop electroosmotic microchannel cooling system for VLSI circuits *IEEE Trans. Comp. Packag. Technol.* **25** 347–55
- [5] Yao S and Santiago J G 2003 Porous glass electroosmotic pumps: theory *J. Colloid Interface Sci.* **268** 133–42
- [6] Yao S, Hertzog D E, Zeng S, Mikkelsen J C and Santiago J G 2003 Porous glass electroosmotic pumps: design and experiments *J. Colloid Interface Sci.* **268** 143–53
- [7] Laser D and Santiago J G 2004 A review of micropumps *J. Micromech. Microeng.* **14** R35–64
- [8] Koch M, Harris N, Evans A, White N and Brunnschweiler A 1998 A novel micromachined pump based on thick-film piezoelectric actuation *Sensors Actuators A* **70** 98–103
- [9] Bourouina T, Bosseboeuf A and Grandchamp J P 1997 Design and simulation of an electrostatic micropump for drug-delivery applications *J. Micromech. Microeng.* **7** 186–8
- [10] Jeong O C and Yang S S 2000 Fabrication and test of a thermopneumatic micropump with a corrugated p plus diaphragm *Sensors Actuators A* **83** 249–55
- [11] Vandepol F, Vanlintel H, Elwenspoek M and Fluitman J 1990 A thermopneumatic micropump based on microengineering techniques *Sensors Actuators A* **21** 198–202
- [12] Gong Q L, Zhou Z Y, Yang Y H and Wang X H 2000 Design, optimization and simulation on microelectromagnetic pump *Sensors Actuators A* **83** 200–7
- [13] Nguyen N T and White R M 1999 Design and optimization of an ultrasonic flexural plate wave micropump using numerical simulation *Sensors Actuators A* **77** 229–36
- [14] Richter A, Plettner A, Hofmann K and Sandmaier H 1991 A micromachined electrohydrodynamic (EHD) pump *Sensors Actuators A* **29** 159–68
- [15] Lemoff A V and Lee P A 2000 An AC magnetohydrodynamic micropump *Sensors Actuators B* **63** 178–85
- [16] Jun T K and Kim C J 1998 Valveless pumping using traversing vapor bubbles in microchannels *J. Appl. Phys.* **83** 5658–64
- [17] Yuan H and Prosperetti A 1999 The pumping effect of growing and collapsing bubbles in a tube *J. Micromech. Microeng.* **9** 402–13
- [18] Ory E, Yuan H, Prosperetti A, Popinet S and Zaleski S 2000 Growth and collapse of a vapor bubble in a narrow tube *Phys. Fluids* **12** 1268–77
- [19] Zahn J D, Deshmukh A A, Pisano A P and Liepmann D 2001 Continuous on-chip micropumping through a microneedle *14th IEEE Int. Conf. on Micro Electro Mechanical Systems (Interlaken, Switzerland 21–25 Jan. 2001)* pp 503–6
- [20] Yin Z and Prosperetti A 2003 A bubble-based micropump, to be submitted
- [21] Allen R R, Meyer J D and Knight W R 1985 Thermodynamics and hydrodynamics of thermal ink jets *Hewlett-Packard J.* **36** 21–7
- [22] Asai A 1991 Bubble dynamics in boiling under high heat flux pulse heating *J. Heat Transfer* **113** 973–9
- [23] Moroney R M, White R M and Howe R T 1991 Ultrasonically induced microtransport *Proc. IEEE MEMS 91* pp 277–82
- [24] Miyazaki S, Kawai T and Araragi M 1991 A piezo-electric pump driven by a flexural progressive wave *Proc. IEEE MEMS 91* pp 283–8
- [25] Kaajakari V, Sathaye A and Lal A 2001 A frequency addressable ultrasonic microfluidic actuator array *Transducers' 01 and Eurosensors XV 11th Int. Conf. on Solid-State Sensors and Actuators (Munich, Germany, 10–14 June, 2001)*
- [26] Gravesen P, Branebjerg J and Jensen O S 1993 Microfluidics—a review *J. Micromech. Microeng.* **3** 168–82
- [27] Brookshier K A and Tarbell J M 1993 Evaluation of a transparent blood analog fluid: aqueous xanthan gum glycerin *Biorheology* **30** 107–16
- [28] Molho J I, Hung C C, Santiago J G, Levine M A and Esch V 2000 Velocity measurements and visualization of the flow driven by laser-induced cavitation bubbles in a blood-like liquid *ASME Int. Mechanical Engineering Congress and Exposition (IMECE) (Orlando, FL, 5–10 Nov., 2000)*
- [29] Riley N 2001 Steady streaming *Ann. Rev. Fluid Mech.* **33** 43–65
- [30] Wang G R, Santiago J G and Mungal M G 2001 Some observation of laser-induced cavitation flow *Bull. Am. Phys. Soc.* **46**
- [31] Hutchins D A 1988 Ultrasonic generation by pulsed lasers *Physical Acoustics* vol 18, ed W P Mason and R N Thurston (New York: Academic) pp 21–123
- [32] Lauterborn W, Kurz T, Mettin R and Ohl C D 1999 Experimental and theoretical bubble dynamics *Adv. Chem. Phys.* **110** 295–380
- [33] Vogel V, Lauterborn W and Timm R 1989 Optical and acoustic investigations of the dynamics of laser-produced cavitation bubbles near a solid boundary *J. Fluid Mech.* **206** 299–338